Research Article J. Electrochem. Sci. Technol., 2021, 12(1), 137-145

# Effect of Iron Species in Mesoporous Fe-N/C Catalysts with Different Shapes on Activity Towards Oxygen Reduction Reaction

Taehong Kang[#], Jiyeon Lee[#], Jong Gyeong Kim, and Chanho Pak*

*Graduate Program of Energy Technology, School of Integrated Technology, Institute of Integrated Technology, Gwangju Institute of Science and Technology, Gwangju, 61005 (Korea)*

**ABSTRACT**

Among the non-precious metal catalysts, iron-nitrogen doped carbon (Fe-N/C) catalysts have been recognized as the most promising candidates for an alternative to Pt-based catalysts for the oxygen reduction reaction (ORR) under alkaline and acidic conditions. In this study, the nano replication method using mesoporous silica, which features tunable primary particle sizes and shape, is employed to prepare the mesoporous Fe-N/C catalysts with different shapes. Platelet SBA-15, irregular KIT-6, and spherical silica particle (SSP) were selected as a template to generate three different kinds of shapes of the mesoporous Fe-N/C catalyst. Physicochemical properties of mesoporous Fe-N/C catalysts are characterized by using small-angle X-ray diffraction, nitrogen adsorption-desorption isotherms, and scanning electron microscopy images. According to the electrochemical evaluation, there is no morphological preference of mesoporous Fe-N/C catalysts toward the ORR activity with half-cell configuration under alkaline electrolyte. By implementing X-ray photoelectron spectroscopy analysis of Fe and N atoms in the mesoporous Fe-N/C catalysts, it is possible to verify that the activity towards ORR highly depends on the portions of "Fe-N" species in the catalysts regardless of the shape of catalysts. It was suggested that active site distribution in the Fe-N/C is one important factor towards ORR activity.

**Keywords :** Non-Precious Metal Catalyst, Mesoporous Fe-N/C Catalyst, Iron-Nitrogen Species, Oxygen Reduction Reaction, Alkaline Electrolyte

*Received : 30 March 2020, Accepted : 17 September 2020*

## 1. Introduction

With an increase in demands for fuel cells, developing efficient non-precious metal catalysts (NPMCs) is a grand challenge in the field of electrochemical catalyst. The oxygen reduction reaction (ORR), a key reaction for fuel cells, is today the most efficiently catalyzed by Pt-based catalyst catalyst [1]. However, there are two major issues when using Pt-based catalysts and their corresponding cathode catalyst layers. One is limited durability caused by abnormal operation condition and impurities in fuel. The other is a high cost [2,3]. There has been no remarkable breakthrough, even though many scientists approach to improve the stability of Pt-based catalysts. Also, the high cost of the Pt-based catalysts still impedes the wide commercialization of fuel cell systems. To address these obstacles, alternative solutions based on inexpensive NMPCs have been investigated for a long time. Of those, iron-nitrogen doped carbon (Fe-N/C) catalysts are regarded as the most promising candidate because of their high ORR activity in both alkaline and acidic electrolytes [4]. At the same time, the alkaline fuel cells (AFCs) have several advantages compared to acidic polymer electrolyte membrane (PEM) fuel cells, e.g., less corrosive environment and more facile kinetics towards ORR with NMPCs [5,6].

Many researchers attempt to elucidate the catalytic active site and their diffusion effect in the Fe-N/C catalysts because a number of active sites and diffusion kinetics influence the ORR activity. There are several synthetic strategies have been developed to

[#]These authors made equal contributions to this work.

*E-mail address: Chanho.pak@gist.ac.kr

DOI: https://doi.org/10.33961/jecst.2020.00892

ascertain them [7-9]. Since recent researches suggest that physical properties of Fe-N/C are deeply related to the ORR activity under acidic condition [10], nano replication method with hard silica template was selected to synthesize Fe-N/C catalysts, which provides the facile control of morphology by the template selection [11,12]. Also, the highly developed porous structures including mesopores [13-16] and micropores are pursued because they feature exposure of large numbers of active sites and subsequently higher catalytic activity towards ORR.

Three types of mesoporous siliceous materials, i.e., SBA-15, KIT-6 and spherical silica particle (SSP) were used as a template of Fe-N/C catalysts, respectively. SBA-15, one of the template materials, has two-dimensional channeling pores arranged in ordered hexagonal (*p6mm*) structure. Because of its adjustable pore size and controllable particle size, SBA-15 has received great attention [17-20]. KIT-6, with the cubic $Ia\bar{3}d$ structural symmetry, is obtained by modifying the mesophase behavior of SBA-15 by adding n-butanol (BuOH) as suggested in the previous literature [21-23]. And it is also attractive because of their ordered three-dimensional channels. SSP has disordered three-dimensional channels, which is easily prepared via the Stöber process by following the previously reported [24,25]. Using these different templates, investigating the effect of morphology and active sites of Fe-N/C catalysts towards ORR was intended.

In this study, three Fe-N/C catalysts were prepared by using three different templates as mentioned above, iron (III) chloride hexahydrate and 1,10-phenanthroline as the precursors for Fe, N and C sources. Their physical properties were characterized by using small-angle X-ray diffraction(XRD) patterning, nitrogen adsorption-desorption isotherms analysis, and their morphological differences were characterized by scanning electron microscopy (SEM) image analysis. The recent study suggests that smaller particle size exerts better ORR activity under acidic conditions [10,26,27], however, morphology effects of the Fe-N/C catalysts on ORR activity were not observed under the alkaline condition in this study. From the XPS analysis, it suggests that the "Fe-N" species is the one significant factor of ORR activity in the half-cell configuration under alkaline conditions.

## 2. Experimental

### 2.1 Preparation of ordered mesoporous silica templates

The Stöber process with a high concentration of tetraethoxyorthosilicate (TEOS) is applied to prepare mesoporous siliceous materials. Conventional rod type SBA-15 is obtained by dissolving non-ionic surfactant, i.e., Pluronic P123 triblock copolymer in 2M HCl solution at 35°C, followed by adding a silica source. In this study, platelet SBA-15 was prepared by adding a small amount of Zr(IV) salt ($ZrOCl_2$) in the rod type SBA-15 starting mixture. Since platelet SBA-15 has relatively shorter mesochannels, it has an advantage in terms of molecular diffusion. The molar composition of the starting gel is 0.017 P123/1 TEOS/0.05 $ZrOCl_2 \cdot 8H_2O$ /7.94 HCl/221 $H_2O$ [17]. The mixture was left under stirring with 300 rates per minute (rpm) at 35°C for 24 h, and subsequently hydrothermally heated at 100°C for another 24 h under static conditions. The precipitated product was isolated by filtration and dried at 80°C for 24 h. After that, the product was calcined in air at 550°C for 3 h [28-31].

As for the KIT-6, it is obtained by adding BuOH as a co-solute. While silica species polymerize along with non-ionic surfactant, the presence of butanol under low HCl concentrations enables the phase controlling and micelle-folding. The molar composition of the starting mixture is 0.017 P123/ 1.2 TEOS/1.31 BuOH/1.83 HCl/195 $H_2O$ [32-36]. Except for adding the n-butanol before adding TEOS, other processes were the same as those of SBA-15.

Lastly, SSP is obtained by using n-hexadecylamine as a non-ionic surfactant. The starting molecular composition for synthesis of SSP is 1 TEOS/ 0.162 n-hexadecylamine/50 IPA/191 $H_2O$ [24]. Deionized water, IPA and n-hexadecylamine were blended for 3 h, and then a certain amount of TEOS was added dropwise at 30°C. The mixture was left under stirring (300 rpm) for 24 h. The precipitated product was isolated by filtration and dried at 80°C for 24 h. After the drying product was corrected by filtration and washed with ethanol (EtOH), the product was calcined in air at 550°C for 3 h.

The preparation of Fe-N/C catalysts was conducted by using the incipient wetness impregnation method [37-40]. Iron (III) chloride hexahydrate and

1,10-phenanthroline were dissolved in sequence in a mixture of EtOH and $H_2SO_4$ solution. Afterward, an equal volume of silica hard template was rubbing vigorously. After evaporation of the solvent, the catalyst precursor powder was dried in an oven at 80°C for 4 h and subsequently dried at 160°C for 12 h. Dried catalyst powder was pyrolyzed at 900°C in Ar for 3 h. In the case of silica host, washing with HF is required to remove the sacrificial template [37-40]. HF filtration should be handled with extreme care. Pyrolyzed powder was filtered and washed with HF, and dried for 24h. The three catalysts are designated as follows: S-Fe-N/C from platelet SBA-15, K-Fe-N/C from KIT-6 and SP-Fe-N/C from SSP, respectively.

### 2.2 Electrochemical measurements

The electrochemical properties were measured with a reference 600 potentiostat in a three-electrode cell equipped with a Pt-wire rod as a counter electrode and a saturated Hg/HgO as a reference electrode. The catalyst ink of Fe-N/C was prepared by dispersing 15 mg of fabricated catalyst in 1.2 mL of Nafion® solution (0.1 mL water, 1.07 mL EtOH and 30 μL of 10 wt.% Nafion® resin). The working electrode was prepared by pipetting 4.75 μL of prepared ink onto the embedded glassy carbon disk of the rotating disk electrode (RDE). Generally, the ORR performance of the catalyst is estimated with an RDE in a half cell setup. The RDE technique allows determining the half-wave potential and the limiting current density, which provides an assessment of the electrochemical catalyst activity [41]. Since the surface area of the glassy carbon disk is 0.196 $cm^2$, 302.93 $\mu g_{catalyst}/cm^2$ catalyst was loaded. The ORR polarization curves were recorded with 5 mV/s and 1600 rpm rotation speed in oxygen saturated 0.1 M KOH electrolyte solution. For comparison, 4 mg of 20 wt.% Pt/C (TKK) was dispersed in 2.4 mL of Nafion® solution (1.99 mL water, 0.5 mL IPA and 10 μL of 10 wt.% Nafion® resin). The prepared ink (29.1 μL) was coated on the glassy carbon surface with 250 $\mu g/cm^2$ of catalyst loading amount. In the durability test, coating conditions Fe-N-C was the same as ORR test, and Pt/C was coated with 100 $\mu g/cm^2$ and 300 $\mu g/cm^2$ respectively for glassy carbon by controlling the drop in the same ink composition. Cycling was performed at 200 mV/s from 0.6 V to 1.0 V under the condition of 0.1 M KOH purged with oxygen.

## 3. Results and Discussion

### 3.1 Characterization of mesoporous silica and Fe-N/C catalysts

The small-angle XRD patterns confirm a structure of template and catalyst. It is widely recognized that the small-angle XRD patterns for SBA-15 structure feature three distinct peaks which are indexable as (100), (110), (200) planes, respectively [42]. The small-angle XRD patterns for both the resultant SBA-15 and S-Fe-N/C shows 3 distinct diffraction peaks as shown in Fig. 1A. Also, small-angle XRD pattern for $Ia\bar{3}d$ cubic symmetry of KIT-6 features has three distinct peaks which are corresponding to (211), (220), (332) planes [33]. However, the resultant K-Fe-N/C from KIT-6 only shows only 1 distinct diffraction peak and a blunt peak $2\theta = 1.2\text{-}1.8^{o}$ (Fig. 1B). Since the presence of mesoporous structures is checked out through nitrogen adsorption-desorption isotherms (Fig. 3B), the absence of 2 distinct peaks may result from amorphous carbon shells generated on the surface [42]. Lastly, SSP is characterized as disorderly pore structures, they give rise to a broad peak in the small-angle XRD as shown in Fig. 1C. In comparison with the silica template, overall shifts of all peaks of Fe-N/C catalyst to higher values of the diffraction angles are observed. This is because that Fe-N/C has the inverse crystalline phase of the mesoporous silica template.

SEM images (Fig. 2) reveal that both the resultant SBA-15 and S-Fe-N/C consist of many platelet type samples of which average width and thickness are about 1 μm and 300 nm, respectively. S-Fe-N/C maintained their template shape, which indicates that hard template synthesis works well. As for the resultant KIT-6 and K-Fe-N/C, they consist of the irregular shape samples of which sizes are much larger (> 10 μm) than that (< 1 μm) of platelet SBA-15. Then, SEM images reveal that the SSP and SP-Fe-N/C consist of many spherical types of domains of which the average diameter is about 1μm.

According to Fig. 3A, the nitrogen adsorption isotherms of the SBA-15 show the classical type IV isotherms with H1 hysteresis loops appeared at which $P/P_0$ is around 0.6-0.8. These types of isotherms are given by mesoporous adsorbents of which pore sizes are between 2 and 50 nm [43]. The average pore size calculated by using the Barrett-Joyner-Halenda (BJH) analysis is 9.36 nm. Hysteresis loops of type

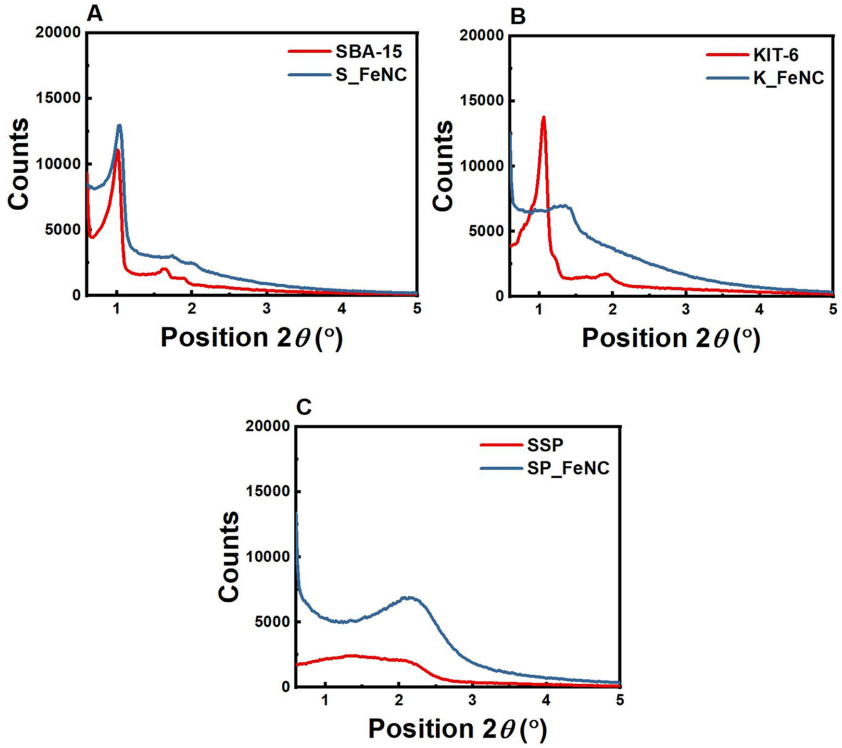


**Fig. 1.** Characterization of physical properties using small-angle XRD: (A) SBA-15 and S-Fe-N/C, (B) KIT-6 and K-Fe-N/C, (C) SSP and SP-Fe-N/C.

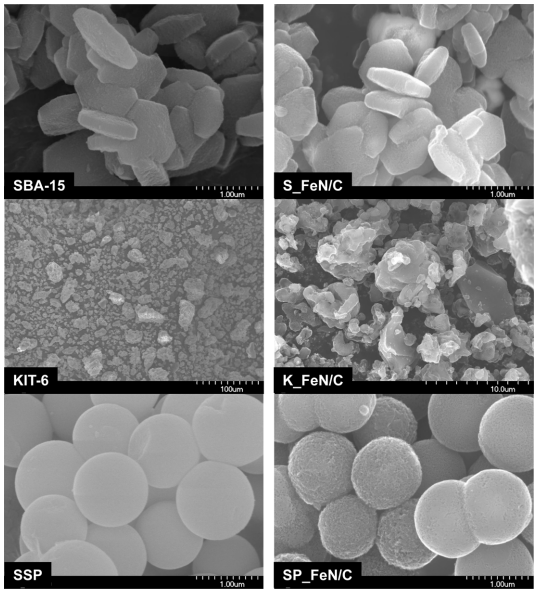


**Fig. 2.** Characterization of morphological properties using SEM images: three types of silica templates and Fe-N/Cs.

H1 are observed in materials that exhibit a narrow range of uniform cylindrical mesopores [28,31]. Also, the specific surface area and pore volume of this material is 719.55 $m^2/g$ and 1.14 $cm^3/g$, respectively. As for the S-Fe-N/C, hysteresis loops appeared at which $P/P_0$ is around 0.5-0.9, which indicates that Fe-N/C consists of mesoporous adsorbents with relatively broad pore size distribution centered at 3.12 nm. The catalyst surface area and pore volume of this material are 1084.7 $m^2/g$ and 0.85 $cm^3/g$.

According to Fig. 3B, the nitrogen adsorption-desorption isotherms of the KIT-6 and K-Fe-N/C show the classical type IV isotherms with H1 and H4 hysteresis loops appeared at which $P/P_0$ is around 0.4-0.9 (Fig. 3B), which implies the existence of mesopore structure in the samples [28,31]. The average pore size calculated by using the BJH method is 9.36 nm. Hysteresis loops of type H1 are given by materials, which exhibit a narrow range of uniform cylindrical mesopores and hysteresis loops of type H4 are associated with slit-like mesopores. Also, the

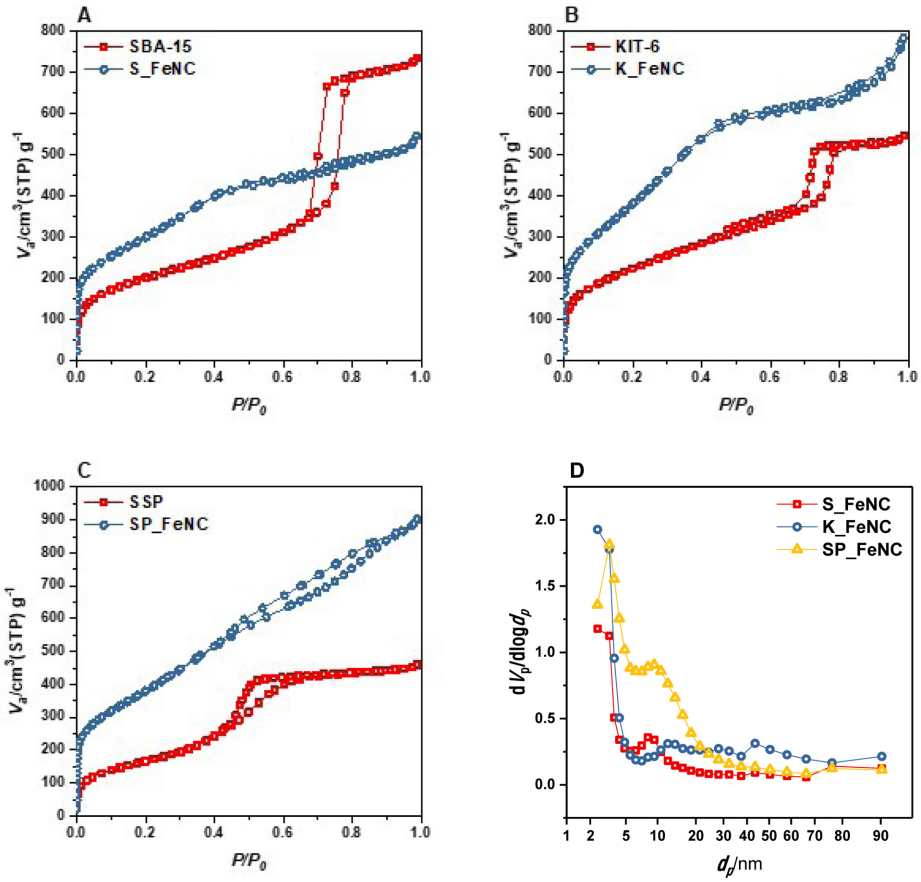


**Fig. 3**. Nitrogen adsorption-desorption isotherms: (A) SBA-15 and S-Fe-N/C, (B) KIT-6 and K-Fe-N/C, (C) SSP and SP-Fe-N/C and (D) Barrett, Joyner and Halenda (BJH) graphs of three types of Fe-N/Cs.

specific surface area and pore volume of KIT-6 is 802.51 $m^2$/g and 0.85 $cm^3$/g, respectively. As for the resultant K-Fe-N/C, hysteresis loops appeared at which $P/P_0$ is around 0.4-1.0, which means that K-Fe-N/C consists of mesoporous adsorbents with relatively broad pore size distribution centered at 3.54 nm. The specific surface area and pore volume of K-Fe-N/C are 1369.7 $m^2$/g and 1.21 $cm^3$/g, respectively.

The nitrogen adsorption-desorption isotherms of the resultant SSP show classical type IV isotherms with H2 hysteresis loops appeared at which $P/P_0$ is around 0.4-0.8 as shown in Fig. 3C. The average pore size calculated by using the BJH method is 4.27nm. Hysteresis loops of type H2 are given by samples that feature the ink-bottle shape of pores. Also, the specific surface area and pore volume of SSP is 609.94 $m^2$/g and 0.71 $cm^3$/g, respectively. As for the SP-Fe-N/C, hysteresis loops appeared at which $P/P_0$ is around 0.4-1.0, which indicates that SP-Fe-N/C consists of mesopores with relatively broad pore size distribution centered at 4.02 nm. In addition, the spe-

**Table 1.** Physical pore properties of three types of Fe-N/C catalysts

| | S-Fe-N/C from SBA-15 | K-Fe-N/C from KIT-6 | SP-Fe-N/C from SSP |
|---|---|---|---|
| Mean Pore diameter (nm) | 3.12 | 3.54 | 4.02 |
| Specific Surface area ($m^2$/g) | 1084.7 | 1369.7 | 1389.4 |
| Total Pore volume ($m^3$/g) | 0.85 | 1.21 | 1.40 |

cific surface area and pore volume of SP-Fe-N/C is 1389.4 $m^2$/g and 1.40 $cm^3$/g, respectively. Nitrogen isotherms data of the three catalysts are summarized in the Table 1. There are some differences between the physical properties of silica templates and those of Fe-N/C. This is because their phases are inversed by the nano-replication method and the constituent materials are different, like silica and carbon [44].

### 3.2 Evaluation of Fe-N/C catalysts toward the ORR

One of the significant ORR activity indicators is a half-wave potential. A half-wave potential is a potential at which current is equal to one half of the diffusion-controlled current. Fig. 4 shows ORR polarization curves of three types of synthesized Fe-N/C catalysts and platinum on carbon (Pt/C, 20wt.% Pt) the catalyst which is a state-of-the-art TKK's commercial catalyst for ORR. All three Fe-N/C catalysts have superior ORR performances than the commercial Pt catalyst in the alkaline condition. However, it seems that there is no morphological preference towards ORR performance in contrast to the previous literature, which suggested the different ORR activity in acidic conditions [26,27]. The half-wave potential of S-Fe-N/C, K-Fe-N/C, and SP-Fe-N/C catalysts is 0.867 V, 0.875 V, and 0.875 V, respectively. Since these values are a little different from each other, it is difficult to judge which catalyst has a better activity towards ORR. Moreover, the recent study suggests that Fe-N/C catalysts prepared by using the KIT-6 template tend to have the worst ORR performance in the acidic condition because of its enormous particle size [26]. However, in this study, K-Fe-N/C features almost the same half-wave potential to the SP-Fe-N/C, but slightly higher potential than the S-Fe-N/C, which implies that K-Fe-N/C catalyst overcame its morphological disadvantages. In the half-cell, the synthesized S-Fe-N/C and the commercial Pt/C were tested for their durability (Fig. S1). The durability of Pt/C was tested with two different loading amounts. One was 100 μg/$cm^2$ and the other was 300 μg/$cm^2$. When measuring 100 μg/$cm^2$ and 300 μg/$cm^2$ of Pt/C, respectively, superior durability at 300 μg/$cm^2$ Pt/C was confirmed. As a result, S-Fe-N/C shifted about 30 mV, whereas only 18 mV shift occurred at 300 μg/$cm^2$ Pt/C in terms of half-wave potential after the test. This result was less than that of a 26 mV shift of 100 μg/$cm^2$ Pt/C, indicating the influence of the loading amount on the catalyst's stability. The durability and

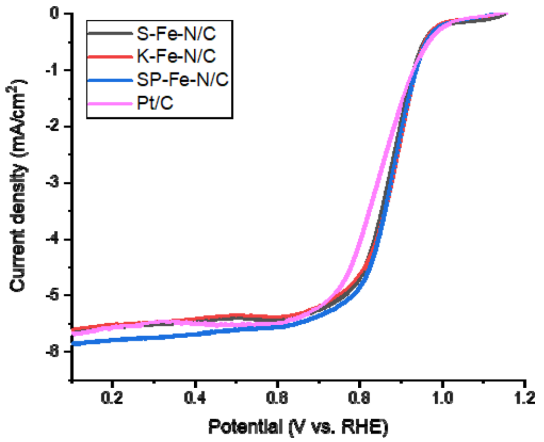


**Fig. 4.** LSV polarization curves of Fe-N/C catalysts and Pt/C (20wt.%) catalyst for the ORR measured using RDE in the alkaline electrolyte (0.1M KOH).

performance difference of catalysts in the half-cell test depending on the loading amount was remarkable in the alkaline medium as precedent studies [45,46]. The decrease in the performance of Pt/C was assumed to be due to the change in surface chemistry, and in the case of Fe-N/C, it was predicted that carbon corrosion occurred due to the relatively low pyrolysis temperature compared to graphitic carbon [47].

To elucidate this result, XPS analysis was implemented in order to analyze the surface atomic states of N and Fe in the catalysts. Actually, the active sites of the Fe-N/C toward the ORR activity are still in controversy [48-52]. So it is expected to get information about active sites if it is possible to investigate what components K-Fe-N/C mostly contains. According to Fig. 5A, a rough outline of the XPS spectrum for K-Fe-N/C is a bit different from those of the others. The distribution of the N component on the right side of Fig. 5A indicates that the three kinds of catalysts have mainly graphitic N (400.8eV) and pyridinic N (398.4eV). Also, both N components are major controversial sites for the ORR activity, respectively. However, there is no obvious clue for the direct relationship of ORR activity from the different portions of two N species. Instead of N species, we concentrate on "Fe-N" bonding and "Fe species" because the amount of Fe component appears to be related to the main active sites in the Fe containing catalysts for ORR [9,51,53,54]. In Fig.

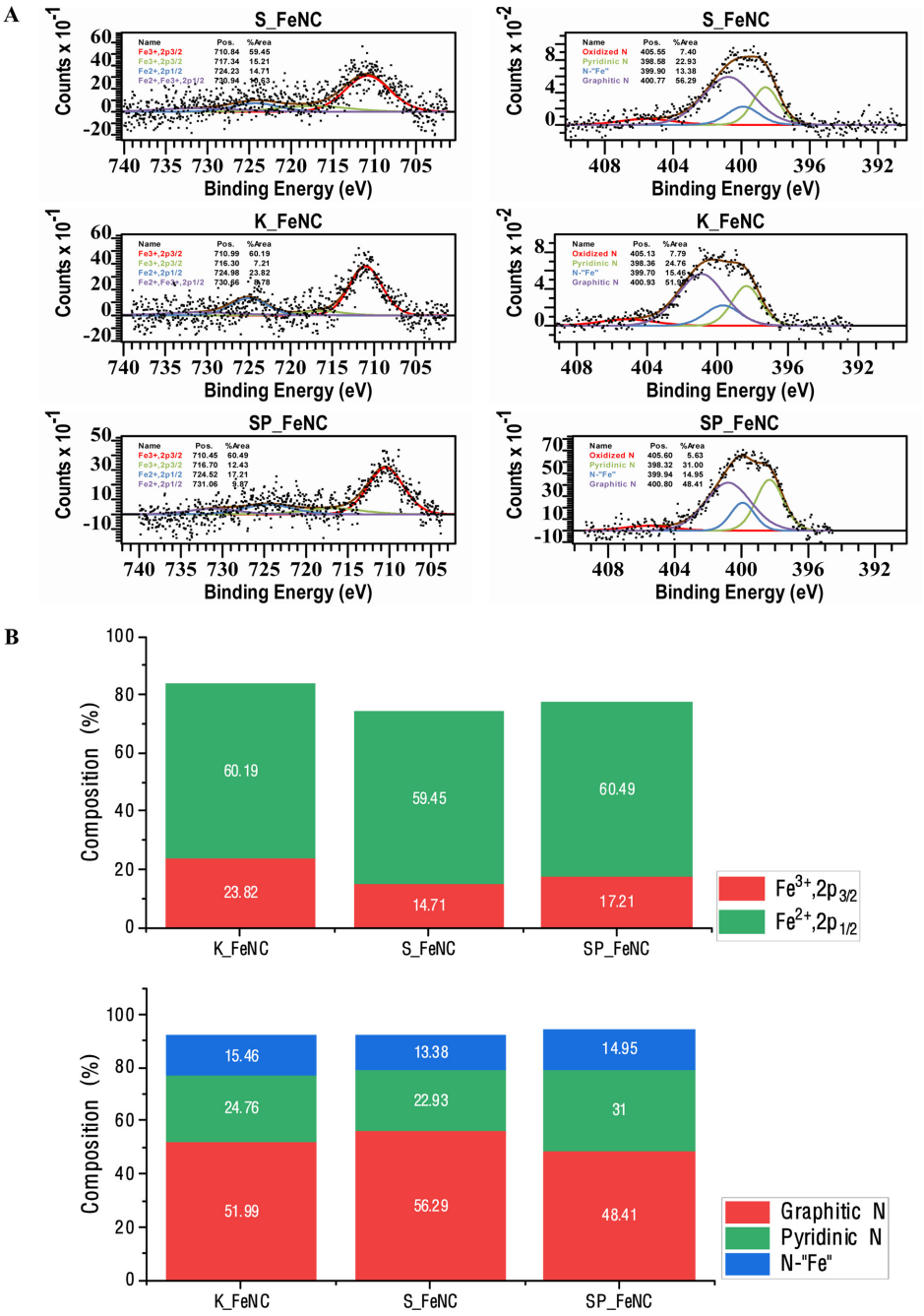


**Fig. 5.** (a) XPS analysis of three types of Fe-N/C catalysts: (Left) Fe 2p regions and (Right) N 1s regions and (b)area percentage of XPS components to Fe 2p and N 1s species.

5B, K-Fe-N/C has the most abundant Fe elements, which contains 7 to 10 at.% more than other catalysts of this study. Also, the state of Fe elements with $Fe^{2+}$ and $Fe^{3+}$ components may affect the performance of the catalyst toward ORR under alkaline conditions. It is expected that the Fe-$N_4$ site would be considered as the main active site in the alkaline non-precious catalyst. This is because the position of the Fe-$N_4$ sites

corresponds to K-Fe-N/C Fe species positions, which is the middle of $Fe^{2+}$ and $Fe^{3+}$ positions [10]. Thus, it is possible to conclude that large numbers of Fe species and Fe-$N_4$ sites, especially $Fe^{2+}$ and $Fe^{3+}$ $2p_{1/2,}$ in K-Fe-N/C as shown in Fig. 5B help to overcome morphological disadvantage in terms of the ORR activity in the half-cell configuration. Thus, it would be suggested that the activity towards ORR of the Fe-N/C catalysts mainly depends on the portion of the Fe species in the catalyst, which can mitigate the size-effect of the Fe containing catalysts in the half-cell configuration.

## 4. Conclusions

In summary, three types of Fe-N/C catalysts were prepared by using mesoporous siliceous materials, i.e., SBA-15, KIT-6, and SSP. The resultant Fe-N/C catalysts feature different pore sizes, surface areas and elemental compounds of a surface. Despite its morphological disadvantage of K-Fe-N/C toward the ORR activity, it features a comparable activity for ORR to the small-sized S-Fe-N/C and SP-Fe-N/C catalysts. And this is because of the existence of large portions of "Fe-N" which is considered as one of the promising candidates of active sites for the ORR. Unfortunately, Fe species XPS is so complex that it is difficult to exactly analyze. However, the results seem to be related to physical properties such as elemental bonding of catalyst compounds as well as morphological properties. Therefore, we should consider both effects when you design ideal catalysts. And the existence of large portions of "Fe-N" sites could be beneficial for promoting the ORR performance in the alkaline condition.

## Acknowledgment

This research was supported by the National Research Foundation of Korea (NRF-2018M1A2A2063174). C. Pak is also thankful for the support from the GIST Research Institute (GRI) grant funded by the GIST in 2020.

## References

[1] (a) C. H. Cui, L. Gan, M. Heggen, S. Rudi and P. Strasser, *Nature Mater.*, **2013**, *12(8)*, 765-771.
(b) L. Sui, W. An, C. K. Rhee, S. H. Hur, *J. Electrochem. Sci. Technol.*, **2020**, *11(1),* 84-91.
[2] C. W. B. Bezerra, L. Zhang, K. Lee, H. Liu, A. L. Marques, E. P. Marques, H. Wang and J. Zhang, *Electrochim. Acta*, **2008**, *53(15)*, 4937-4951.
[3] S. Gottesfeld, D. R. Dekel, M. Page, C. Bae, Y. S. Yan, P. Zelenay and Y. S. Kim, *J. Power Sources*, **2018**, *375*, 170-184.
[4] Y. J. Sa, J. H. Kim, S. H. Joo, *J. Electrochem. Sci. Technol.*, **2017**, *8(3)*, 169-182.
[5] X. Li, B. N. Popov, T. Kawahara and H. Yanagi, *J. Power Sources*, **2011**, *196(4)*, 1717-1722.
[6] D. R. Dekel, *J Power Sources*, **2018**, *375*, 158-169.
[7] S. Maurya, C. H. Fujimoto, M. R. Hibbs, C. N. Villarrubia and Y. S. Kim, *Chem. Mater.*, **2018**, *30(7)*, 2188-2192.
[8] K. S. Park, S.-A. Jin, K. H. Lee, J. Lee, I. Song, B. S. Lee, S. Kim, J. Sohn, C. Pak, G. Kim, S. G. Doo and K. Kwon, *Int. J. Electrochem Sci.*, **2016**, *11(11)*, 9295-9306.
[9] P. H. Matter, L. Zhang and U. S. Ozkan, *J. Catal.*, **2006**, *239(1)*, 83-96.
[10] H. Zhang, S. Hwang, M. Wang, Z. Feng, S. Karakalos, L. Luo, Z. Qiao, X. Xie, C. Wang, D. Su, Y. Shao and G. Wu, *J. Am. Chem. Soc.*, **2017**, *139(40)*, 14143-14149.
[11] E. Rossinyol, J. Arbiol, F. Peiro, A. Cornet, J. R. Morante, B. Tian, T. Bo and D. Zhao, *Sensors and Actuators B: Chem.*, **2005**, *109(1)*, 57-63.
[12] E. Luo, M. Xiao, Y. Wang, J. Ge, C. Liu and W. Xing, *ChemCatChem*, **2018**, *10(17)*, 3653-3658.
[13] L. Fan, P. Sun, L. Yang, Z. Xu and J. Han, *Korean J. Chem. Eng.*, **2020**, *37(1)*, 166-175.
[14] H. Burri, R. Anjurn, R. B. Gurram, H. Mitta, S. Mutyala and M. Jonnalagadda, *Korean J. Chem. Eng.*, **2019**, *36(9)*, 1482-1488.
[15] S. Wang, L. Lyu, G. Sima, Y. Cui, B. Li, X. Zhang and L. Gan, *Korean J. Chem. Eng.*, **2019**, *36(7)*, 1042-1050.
[16] S. Ghosh, W. D. Yong, E. M. Jin, S. R. Polaki, S. M. Jung and H. Jun, *Korean J. Chem. Eng.*, **2019**, *36(2)*, 312-320.
[17] S.-Y. Chen, C.-Y. Tang, W.-T. Chuang, J.-J. Lee, Y.-L. Tsai, J. C. C. Chan, C.-Y. Lin, Y.-C. Liu and S. Cheng, *Chem. Mater.*, **2008**, *20(12)*, 3906-3916.
[18] X. Jin, C. H. Lee, J. H. Kim, D. J. You, C. Pak, J. K. Shonand J. M. Kim, *Bull. Korean Chem. Soc.*, **2015**, *36(8)*, 2062-2067.
[19] S. H. Joo, H. I. Lee, D. J. You, K. Kwon, J. H. Kim, Y. S. Choi, M. Kang, J. M. Kim, C. Pak, H. Chang and D. Seung, *Carbon*, **2008**, *46(15)*, 2034-2045.
[20] S. C. Ryu, J. H. Lee and H. Moon, *Korean J. Chem. Eng.*, **2019**, *36(9)*, 1410-1416.
[21] F. Kleitz, T. W. Kim and R. Ryoo, *Bull. Korean Chem. Soc.*, **2005**, *26(11)*, 1653-1668.
[22] J. K. Shon, H. S. Lee, G. O. Park, J. Yoon, E. Park, G. S. Park, S. S. Kong, M. Jin, J.-M. Choi, H. Chang, S. Doo, J. M. Kim, W.-S. Yoon, C. Pak, H. Kim and G. D. Stucky, *Nature Commun.*, **2016**, *7(1)*, 11049.
[23] W. Cai, Q. Chen, H. Xuan, C. Li, H. yu, L. Cui, Z. Yu, S. Zhang and F. Qu, *Korean J. Chem. Eng.*, **2019**, *36(4)*,

513-521.
[24] Y. He, H. Xu, S. Ma, P. Zhang, W. Huang and M. Kong, *Mater. Lett.*, **2014**, *131*, 361-365.
[25] X.-D. Wang, Z.-X. Shen, T. Sang, X.-B. Cheng, M.-F. Li, L.-Y. Chen and Z.-S.Wang, *J. Colloid Interface Sci.*, **2010**, *341(1)*, 23-29.
[26] J. Woo, Y. J. Sa, J. H. Kim, H. W. Lee, C. Pak and S. H. Joo, *ChemElectroChem*, **2018**, *5(14)*, 1928-1936.
[27] U. Byambasuren, Y. Jeon, D. Altansukh, Y. Ji and Y.-G. Shul, *Korean J. Chem. Eng.*, **2016**, *33(6)*, 1831-1836.
[28] M. Kruk, M. Jaroniec, S. H. Joo and R. Ryoo, *J. Phys. Chem. B*, **2003**, *107(10)*, 2205-2213.
[29] H. I. Lee, J. H. Kim, G. D. Stucky, Y. Shi, C. Pak and J. M. Kim, *J. Mater. Chem.*, **2010**, *20(39)*, 8483-8487.
[30] D. Zhao, J. Feng, Q. Huo, N. Melosh, G. H. Fredrickson, B. F. Chmelka and S. D. Stucky, *Science*, **1998**, *279(5350)*, 548-552.
[31] J. M. Esparza, M. L. Ojeda, A. Campero, A. Domínguez, I. Kornhauser, F. Rojas, A. M. Vidales, R. H. López and G. Zgrablich, *Colloids and Surfaces A: Physicochem. Eng. Aspects*, **2004**, *241(1-3)*, 35-45.
[32] R. Atchudan, J. Joo and A. Pandurangan, *Mater. Res. Bull.*, **2013**, *48(6)*, 2205-2212.
[33] H. I. Lee, G. D. Stucky, J. H. Kim, C. Pak, H. Chang and J. M. Kim, *Adv. Mater.*, **2011**, *23(20)*, 2357-2361.
[34] W. Guo, F. Kleitz, K. Cho and R. Ryoo, *J. Mater. Chem.*, **2010**, *20(38)*, 8257-8265.
[35] C. Jo, K. Kim and R. Ryoo, *Micropo. Mesopo. Mater.*, **2009**, *124(1-3)*, 45-51.
[36] D. H. Choi and R. Ryoo, *J. Mater. Chem.*, **2010**, *20(26)*, 5544-5550.
[37] H. Chang, S. H. Joo and C. Pak, *J. Mater. Chem.*, **2007**, *17(30)*, 3078-3088.
[38] S. H. Joo, C. Pak, D. J. You, S. A. Lee, H. I. Lee, J. M. Kim, H. Chang and D. Seung, *Electrochim. Acta*, **2006**, *52(4)*, 1618-1626.
[39] C. Pak, S. J. Lee, S. A. Lee and H. Chang, *Korean J. Chem. Eng.*, **2005**, *22(2)*, 214-218.
[40] H. I. Lee, J. H. Kim, D. J. You, J. E. Lee, J. M. Kim, W.-S. Ahn, C. Pak, S. H. Joo, H. Chang and D. Seung, *Adv. Mater.*, **2008**, *20(4)*, 757-762.
[41] N. Daems, T. Breugelmans, I. F. J. Vankelecom and P. P. Pescarmona, *ChemElectroChem*, **2018**, *5(1)*, 119-128.
[42] J. Y. Cheon, C. Ahn, D. J. You, C. Pak, S. H. Hur, J. Kim and S. H. Joo, *J. Mater. Chem. A*, **2013**, *1(4)*, 1270-1283.
[43] M. Thommes, K. Kaneko, A. V. Neimark, J. P. Olivier, F. Rodriguez-Reinoso, J. Rouquerol and K. S. W. Sing, *Pure Appl. Chem.*, **2015**, *87(9-10)*, 1051-1069.
[44] U. Byambasuren, Y. Jeon, D. Altansukh, Y. Ji and Y.-G. Shul, *Carbon Lett.*, **2016**, *17(1)*, 53-64.
[45] N. Du, C. Wang, R. Long and Y. Xiong, *Nano Res.* **2017**, *10(9)*, 3228−3237.
[46] Y. Feng, Q. Shao, Y. Ji, X. Cui, Y. Li, X. Zhu, X. Huang, *Sci. Adv.* **2018**, *4(7)*, eaap8817.
[47] A. Zadick, L. Dubau, N. Sergent, G. Berthomé, and M. Chatenet, *ACS. Catal.* **2015**, *5(8)*, 4819−4824.
[48] M. Li, F. Xu, H. Li and Y. Wang, *Catal. Sci. Tech.*, **2016**, *6(11)*, 3670-3693.
[49] C. H. Choi, W. S. Choi, O. Kasian, A. K. Mechler, M. T. Sougrati, S. Brüller, K. Strickland, Q. Jia, S. Mukerjee, K. J. J. Mayrhofer and F. Jaouen, *Angew. Chem. Int. Ed.*, **2017**, *56(30)*, 8809-8812.
[50] L.-B. Lv, S.-Z. Yang, W.-Y. Ke, H.-H. Wang, B. Zhang, P. Zhang, X.-H. Li, M. F. Chisholm and J.-S. Chen, *ChemCatChem*, **2018**, *10(16),* 3539-3545.
[51] K. Mamtani, D. Jain, A. C. Co and U. S. Ozkan, *Energy Fuels*, **2017**, *31(6)*, 6541-6547.
[52] Y. Qiao, P. Yuan, Y. Hu, J. Zhang, S. Mu, J. Zhou, H. Li, H. Xia, J. He and Q. Xu, *Adv. Mater.*, **2018**, *30(46)*, 1804504.
[53] M. M. Hossen, K. Artyushkova, P. Atanassov and A. Serov, *J. Power Sources*, **2018**, *375*, 214-221.
[54] S. Ganesan, N. Leonard and S. C. Barton, *Phys. Chem. Chem. Phys.*, **2014**, *16(10)*, 4576-4585.